water

MDPI

Supplementary Information

Enhanced Photo-Fenton Activity Using Magnetic $Cu_{0.5}Mn_{0.5}Fe_2O_4$ Nanoparticles as a Recoverable Catalyst for Degrading Organic Contaminants

Athaphon Angkaew [1], Chainarong Sakulthaew [2], Matura Nimtim [1], Saksit Imman [3], Tunlawit Satapanajaru [1], Nopparat Suriyachai [3], Torpong Kreetachat [3], Steve Comfort [4] and Chanat Chokejaroenrat [1,*]

Section S1. Chemicals

The chemicals used in this research were analytical grade and were purchased from several vendors. Manganese sulfate monohydrate ($MnSO_4 \cdot H_2O$) was purchased from Loba Chemie Pvt. Ltd. (Mumbai, India). Ferric chloride hexahydrate ($FeCl_3 \cdot 6H_2O$) and acetic acid were obtained from QRëC (Auckland, New Zealand). Sodium hydroxide (NaOH), hydrogen peroxide (30%, H_2O_2), copper sulfate ($CuSO_4$), oxytetracycline dihydrate ($C_{22}H_{24}N_2O_9 \cdot 2H_2O$; OTC), enrofloxacin ($C_{19}H_{22}FN_3O_3$; ENR), sulfadimethoxine sodium salt ($C_{12}H_{13}N_4O_4SNa$; SDM) and sulfamethoxazole ($C_{10}H_{11}N_3O_3S$; SMX), methyl 4-hydroxybenzoate ($C_8H_8O_3$; methylparaben), propyl 4-hydroxybenzoate ($C_{10}H_{12}O_3$; propylparaben), butyl 4-hydroxybenzoate ($C_{11}H_{14}O_3$; butylparaben) were purchased from Merck (Darmstadt, Germany). Tert-butanol ($C_4H_{10}O$; TBA) was purchased from Carlo Erba (Val-de-Reuil, France). Dimethyl sulfoxide (C_2H_6OS; DMSO), acetonitrile (C_2H_3N; ACN) and methanol (CH_3OH; MeOH) were purchased from RCI Labscan (Bangkok, Thailand). Ethyl alcohol anhydrous (C_2H_5OH; EtOH) was purchased from Daejung (Gyeonggi, Korea). Melamine ($C_3H_6N_6$), ethyl 4-hydroxybenzoate ($C_9H_{10}O_3$; ethylparaben), and p-benzoquinone ($C_6H_4O_2$; pBQ) were purchased from Alfa Aesar (Shanghai, China). Atrazine ($C_8H_{14}ClN_5$; ATZ) was purchased from Dr. Ehrenstorfer GmbH (Augsburg, Germany). Alachlor ($C_{14}H_{20}ClNO_2$; ALA) was obtained from Chem Service (Pennsylvania, United States). 2,4 dichlorophenoxyacetic acid ($C_8H_6Cl_2O_3$; 2,4-D) was obtained from Spectrum (New Jersey; United States). Methylene blue ($C_{16}H_{18}ClN_3S \cdot 2H_2O$; MB) and methyl orange ($C_{14}H_{14}N_3NaO_3S$; MO) were purchased from Ajax Finechem (Auckland, New Zealand). Crystal violet ($C_{25}N_3H_{30}Cl$; CV) was obtained from Vidhyasom (Bangkok, Thailand). Deionized water (DI) was used in all experiments.

Section S2. Chemical analyses

The concentration of antibiotics, herbicides, and parabens were quantified by high-performance liquid chromatography (HPLC; 600E Waters, Milford, MA, USA) equipped with a UV detector (2487, Waters, Milford, MA). We used two HPLC C18 analytical columns: (1) Mightysil, RP-18 GP 250 x 4.6 (5 μm) for antibiotic analysis, and (2) Phenomenex, Luna 5u C18(2), 250 x 4.6 mm) (5 μm) for herbicide and paraben analyses. Details of HPLC condition such as mobile phase ratio, flow rate, and the detection wavelength for determining each pollutant were presented in Table S1. The concentration of methylene blue (MB), methyl orange (MO) and crystal violet (CV) were quantified using a UV-Vis spectrophotometer (libra S6, Biochrom, England) at the wavelength of 665, 464, and 585 nm. Total organic carbon (TOC) and total nitrogen (TN) concentrations were quantified using a total organic carbon analyzer (TOC-L; H544258, Shimadzu, Japan) equipped with a total nitrogen measuring unit (TNM-L; H564058, Shimadzu, Japan). The concentration of leaching metals (Cu, Mn and Fe) was determined using a flame atomic absorption spectrophotometer (FAAS; 200AA, Agilent). The turbidity and water parameters (pH, total dissolved solids, conductivity and salinity) were measured using a turbidity meter (Turb 430IR,

WTW, Weilheim, Germany) and a multi-parameter analyzer (C1020, Consort, Turnhout, Belgium).

Section S3. Material characterization

In this work, the catalysts were characterized by several instruments. We investigated the crystal structure by an X-ray diffractometer (XRD; D2 phaser, Bruker, Berlin, Germany) with Cu Kα radiation (l=0.15406 nm). The magnetic properties were determined using a vibrating sample magnetometer (VSM; custom-made by the Department of Physics, Kasetsart University, Bangkok, Thailand). The surface functional groups were analyzed by Fourier transform infrared spectroscopy (FTIR; Tensor 27, Bruker, Berlin, Germany). The surface chemical compositions and chemical state changes were analyzed by X-ray photoelectron spectroscopy (XPS; Kratos, AXIS ultra DLD, Manchester, England) occupied with the VISION II software. The morphological structures were observed by scanning electron microscopy (SEM; JEOL, JSM-6010, Tokyo, Japan) and high-resolution transmission electron microscopy (HRTEM; Talos F200X, Thermo Scientific, USA). The optical properties were determined by UV-Vis diffuse reflectance spectrophotometer (UV-Vis-DRS; Cary 300, Agilent).

Section S4. Role of melamine addition

Based on XRD results, we did not observe the existence of melamine and/or graphitic carbon nitride (g-C_3N_4; a polymer resulted from melamine polymerization under high temperatures) in the $Cu_{0.5}Mn_{0.5}Fe_2O_4$ XRD spectra (e.g., at $2\theta = 13.1°$ and 27.4°), which was possibly due to the minimal melamine content used in the process. Despite this disappearance, we believed that the g-C_3N_4 was formed and acted as a coordinating agent during the calcination process and may further decompose at 550°C, which was consistent with results reported by [1,2].

To elucidate the melamine role, we used FTIR to determine the surface chemical composition and compare the catalyst spectral changes with and without melamine addition. Both FTIR spectra showed absorption peaks around 400-600 cm^{-1} which can be ascribed to the metal-oxygen bonds (Fe-O, Mn-O, and Cu-O) [3,4] (Figure S2a). Without melamine addition, there were high-intensity peaks at 1395, 1530, and 1641 cm^{-1}, which can be attributed to C-O, C=O, and C=C bonds [5,6]. While with melamine addition, we observed a stronger M-O absorption peak (540 cm^{-1}), the C-O and C=O bond disappearance, and no nitrogen-containing bond peaks. This was due to the coprecipitated particle-melamine complex sublimation occurred during the calcination process. Once melamine was heated with the coprecipitated particles, it provided a platform for homogeneous distribution of nanoparticles, and coordinated to the transition metals, resulting in the metal-melamine complex formation [7,8]. Under the high calcining temperature (550°C), this complex can further decompose into spinel ferrite structure and volatile gases (i.e., CO_x, NO_x, and NH_3) [9]. This confirmed the melamine role as a coordinating agent that can improve the $Cu_{0.5}Mn_{0.5}Fe_2O_4$ crystallinity and successfully prevent the -Fe_2O_3 formation.

Following the $Cu_{0.5}Mn_{0.5}Fe_2O_4$ catalytic treatment, we measured the catalyst elemental composition and metal oxidation states using XPS. The survey scan XPS spectra verified the C, O, Mn, Fe, and Cu presence at the 285, 530, 641, 711, and 935 eV binding energy (Figure S2b). In the C 1s spectra, the peaks at 282.8 and 283.8 eV were ascribed to M-C bonds, and the other peaks at 284.9, 286.3, and 288.4 eV were attributed to C-C/C=C, C-O, and O=C-O (Figure S2c) [3,5]. Although the g-C_3N_4 character was not present in the XRD, FTIR, and XPS results, the C 1s spectra showed the M-C and C-C/C=C bonds (Figure S2c). The absence of g-C_3N_4 (i.e., C-N) can be explained from the small melamine content during calcination and the high ferrite dispersion, which may overshadow the g-C_3N_4 [2]. Furthermore, the g-C_3N_4 decomposition temperature (~630°C) may shift to <550°C, causing the particle-melamine complex and g-C_3N_4 that conjugated with metal oxide to decompose. However, the carbon content remnant from melamine could still be decorated

on the catalyst, corresponding to the M-C and C-C/C=C bond formation. Like carbon-based material doping, these carbons could act as an electron acceptor, forming a hetero-junction structure with $Cu_{0.5}Mn_{0.5}Fe_2O_4$ which could enhance the light absorption capability and suppress photo-excited electron-hole recombination, thereby improving $Cu_{0.5}Mn_{0.5}Fe_2O_4$ photocatalytic activity [10,11].

Table S1. HPLC conditions for quantifying the concentrations of antibiotics, herbicides, and parabens.

Pollutants	Mobile phase (%)			Flow rate (mL/min)	Wavelength (nm)	Retention time (min)
	Acetonitrile	Acetic acid (0.1% v/v)	H_2O			
Oxytetracycline	20	80	-	1	354	~4.6
Enrofloxacin	20	80	-	1	270	~4.5
Sulfadimethoxine	60	40	-	1	270	~3.8
Sulfamethoxazole	60	40	-	1	270	~3.5
Alachlor	75	-	25	1	200	~7
Atrazine	75	-	25	1	220	~4.5
2,4-Dichlorophenoxyacetic acid	75	-	25	1	200	~1.9
Methyl-paraben	60	-	40	1	254	~3.9
Ethyl-paraben	60	-	40	1	254	~4.6
Propyl-paraben	60	-	40	1	254	~5.7
Buthyl-paraben	60	-	40	1	254	~7.5

Table S2. Physical and chemical characteristics of the water samples.

Parameter	Unit	Influent wastewater	Effluent wastewater	Wastewater Station #1	Wastewater Station #2	Canal water	Wastewater Station #3
pH	-	7.0	6.9	7.2	7.0	7.0	7.1
Conductivity	µS/cm	550.0	535.0	448.0	462.0	329.0	491.0
TDS	mg/L	289.0	280.0	239.0	246.0	175.0	259.0
Salinity	PSU	0.3	0.3	0.2	0.2	0.2	0.2
Turbidity	NTU	5.00	12.00	3.50	6.00	15.50	12.2
UV_{254}	Absorbance	0.1550	0.1740	0.1370	0.3600	0.2710	-
TC	mg/L	53.33	50.71	43.88	53.72	40.36	53.17
TOC	mg/L	8.79	7.98	8.41	11.68	8.95	13.74
TN	mg/L	7.24	7.36	6.07	2.62	1.78	5.86
Before treating (adding OTC)							
Turbidity	NTU	5.00	11.50	3.75	6.20	15.70	-
TC	mg/L	73.35	71.84	66.53	76.49	63.36	-
TOC	mg/L	36.06	33.94	35.43	37.85	34.65	-
TN	mg/L	9.94	9.86	8.85	5.48	4.60	-
After treating							
Turbidity	NTU	0.01	2.00	0.50	0.17	4.00	-
TC	NTU	40.40	46.27	44.29	42.07	41.61	-
TOC	mg/L	22.79	23.59	23.44	27.62	26.03	-
TN	mg/L	5.409	5.622	6.36	3.802	3.812	-

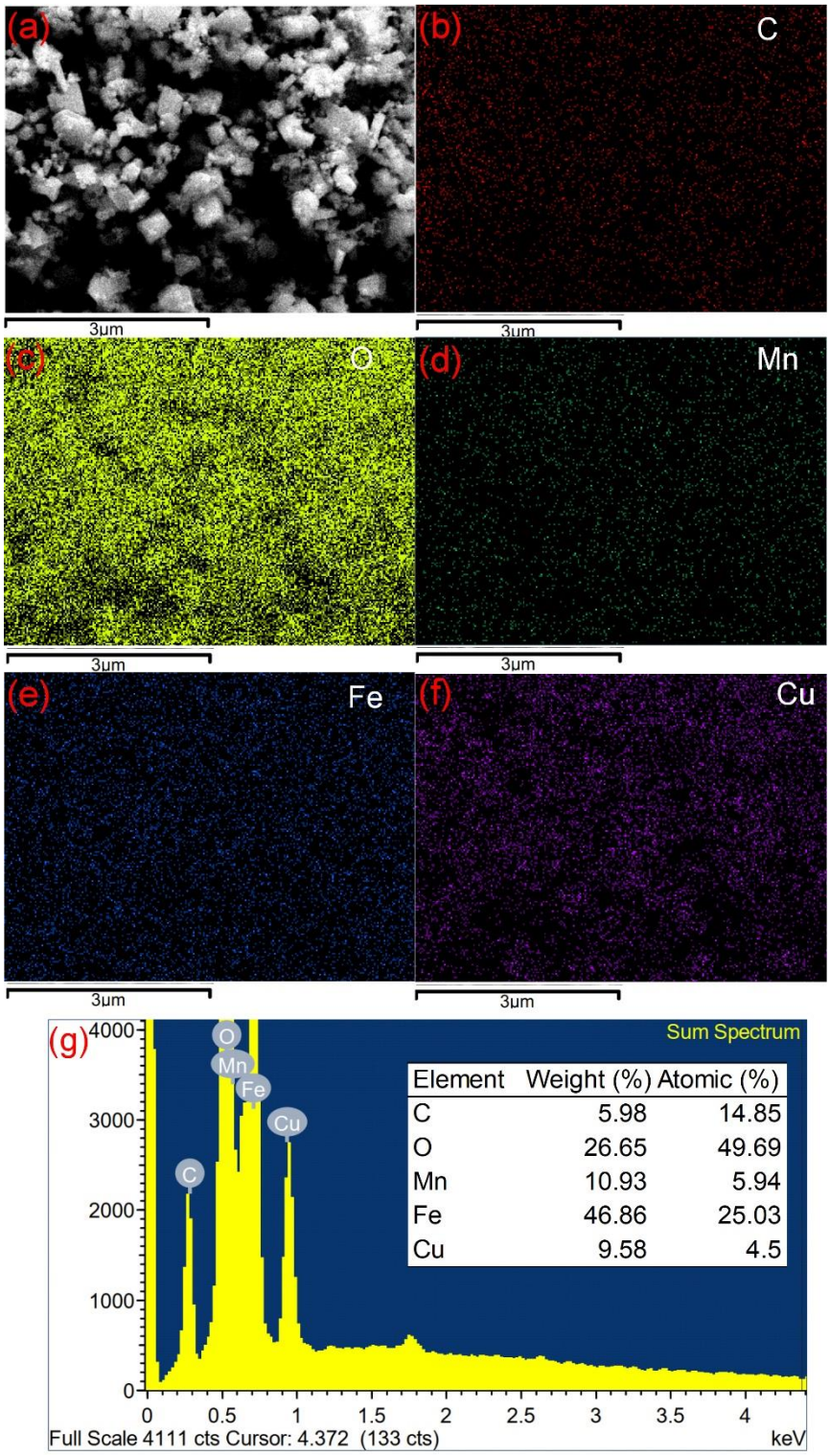

Figure S1. (a) scanning electron microscopy (SEM)image, X-ray mapping of (b) C, (c) O, (d) Mn, (e) Fe, (f) Cu and (g) spectrum of $Cu_{0.5}Mn_{0.5}Fe_2O_4$ nanoparticles.

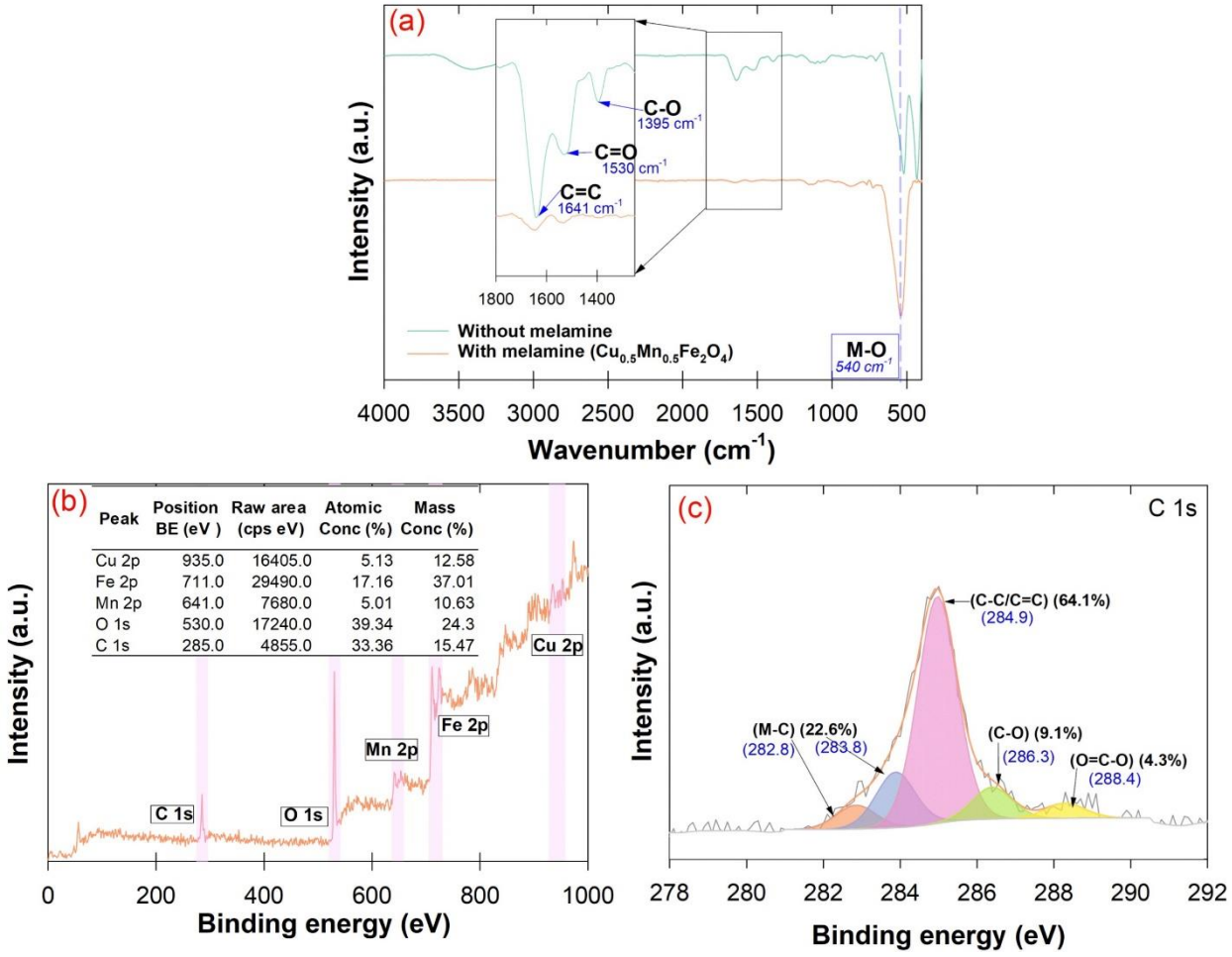

Figure S2. The $Cu_{0.5}Mn_{0.5}Fe_2O_4$ nanoparticle (a) FTIR, (b) XPS survey, (c) C 1s XPS spectra.

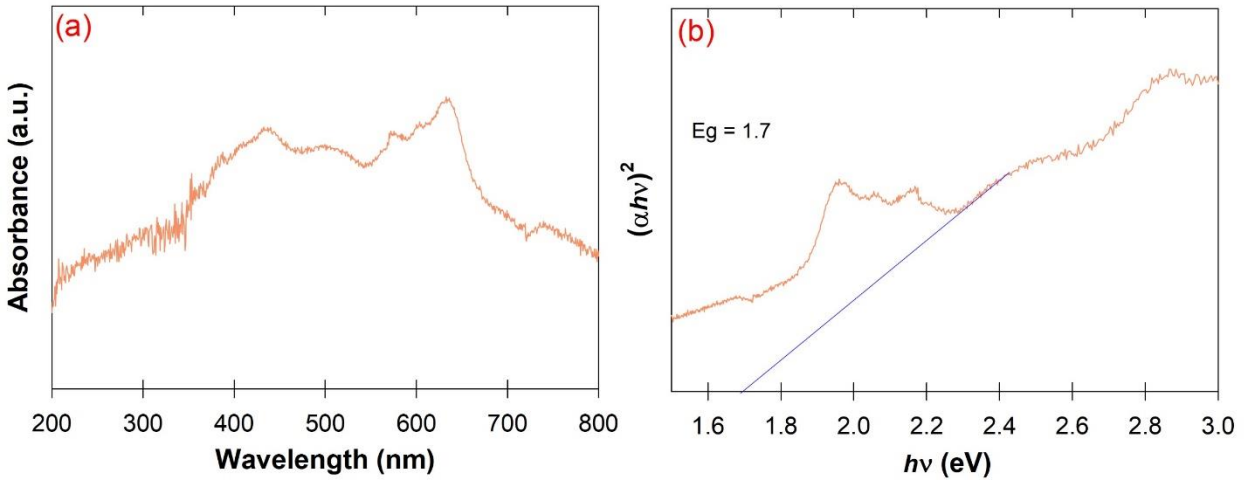

Figure S3. (a) UV-Vis diffuse reflectance spectra (DRS), (b) $(\alpha h\nu)^2$ vs. photon energy ($h\nu$) curves of the $Cu_{0.5}Mn_{0.5}Fe_2O_4$ nanoparticles.

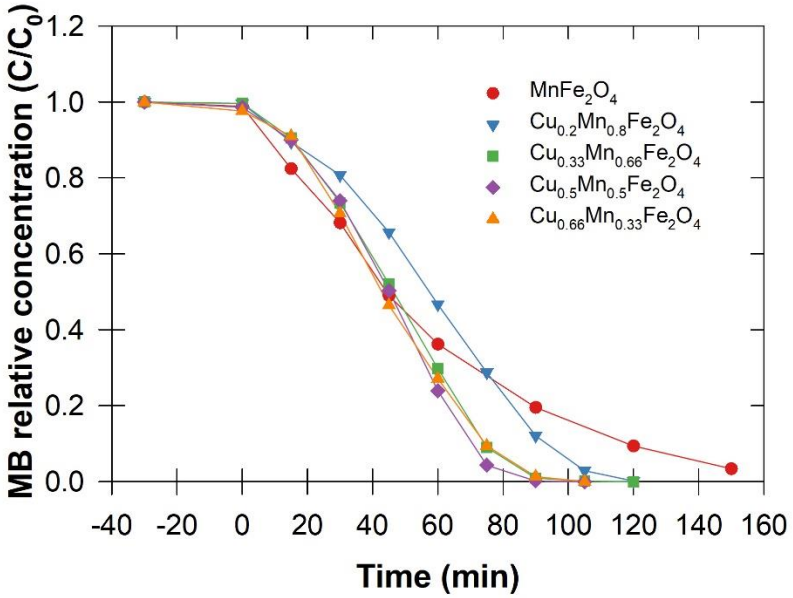

Figure S4. Photo-Fenton catalytic degradation of MB with different composition ratios (Conditions: $[H_2O_2]$ = 97.89 mM, catalyst loading = 0.5 g/L, $[MB]_0$ = 80 mg/L).

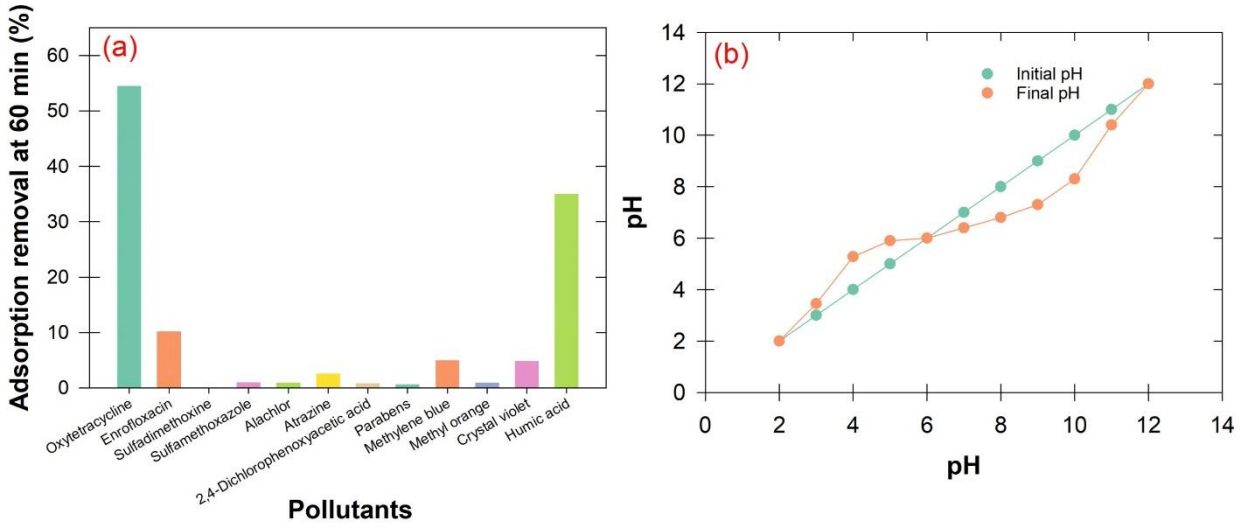

Figure S5. (a) Adsorption of various organic pollutants by $Cu_{0.5}Mn_{0.5}Fe_2O_4$ nanoparticles (Conditions: catalyst dose = 4 g/L, $[pollutant]_0$ = 0.1 mM or $[HA]_0$ = 100 mM) and (b) pH_{pzc} analysis of $Cu_{0.5}Mn_{0.5}Fe_2O_4$ nanoparticles.

References

1. Huang, L.; Xu, H.; Li, Y.; Li, H.; Cheng, X.; Xia, J.; Xu, Y.; Cai, G. Visible-light-induced WO_3/g-C_3N_4 composites with enhanced photocatalytic activity. *Dalton Transactions* **2013**, *42*, 8606–8616. https://doi.org/10.1039/C3DT00115F.
2. Huang, S.; Xu, Y.; Xie, M.; Xu, H.; He, M.; Xia, J.; Huang, L.; Li, H. Synthesis of magnetic $CoFe_2O_4$/g-C_3N_4 composite and its enhancement of photocatalytic ability under visible-light. *Colloids and Surfaces A: Physicochemical and Engineering Aspects* **2015**, *478*, 71–80. https://doi.org/10.1016/j.colsurfa.2015.03.035.
3. Wang, Z.; Lai, C.; Qin, L.; Fu, Y.; He, J.; Huang, D.; Li, B.; Zhang, M.; Liu, S.; Li, L.; et al. ZIF-8-modified $MnFe_2O_4$ with high crystallinity and superior photo-Fenton catalytic activity by Zn-O-Fe structure for TC degradation. *Chemical Engineering Journal* **2020**, *392*, 124851. https://doi.org/10.1016/j.cej.2020.124851.
4. Ghassemi, N.; Davarani, S.S.H.; Moazami, H.R. Cathodic electrosynthesis of $CuFe_2O_4$/CuO composite nanostructures for high performance supercapacitor applications. *Journal of Materials Science: Materials in Electronics* **2018**, *29*, 12573–12583. https://doi.org/10.1007/s10854-018-9374-8.

5. Lai, C.; Huang, F.; Zeng, G.; Huang, D.; Qin, L.; Cheng, M.; Zhang, C.; Li, B.; Yi, H.; Liu, S. Fabrication of novel magnetic $MnFe_2O_4$/bio-char composite and heterogeneous photo-Fenton degradation of tetracycline in near neutral pH. *Chemosphere* **2019**, *224*, 910–921. https://doi.org/10.1016/j.chemosphere.2019.02.193.
6. Ghobadi, M.; Gharabaghi, M.; Abdollahi, H.; Boroumand, Z.; Moradian, M. $MnFe_2O_4$-graphene oxide magnetic nanoparticles as a high-performance adsorbent for rare earth elements: Synthesis, isotherms, kinetics, thermodynamics and desorption. *Journal of Hazardous Materials* **2018**, *351*, 308–316. https://doi.org/10.1016/j.jhazmat.2018.03.011.
7. M. L. Goodgame, D.; Hussain, I.; J. P. White, A.; J. Williams, D. Synthesis and structure of a copper(II) melamine complex, $[Cu(C_3H_6N_6)(\mu\text{-}OCH_3)(ONO_2)(HOCH_3)]_2$, with direct Cu–melamine coordination. *Journal of the Chemical Society, Dalton Transactions* **1999**, 2899-2900. https://doi.org/10.1039/A905576B.
8. Wiles, A.B.; Bozzuto, D.; Cahill, C.L.; Pike, R.D. Copper (I) and (II) complexes of melamine. *Polyhedron* **2006**, *25*, 776–782. https://doi.org/10.1016/j.poly.2005.08.022.
9. Doddamani, J.S.; Hodlur, R.M.; Rabinal, M.K. Melamine assisted large-scale and rapid synthesis of porous copper oxide nanostructures. *Emergent Materials* **2021**. https://doi.org/10.1007/s42247-021-00250-1.
10. Ansari, S.A.; Ansari, S.G.; Foaud, H.; Cho, M.H. Facile and sustainable synthesis of carbon-doped ZnO nanostructures towards the superior visible light photocatalytic performance. *New Journal of Chemistry* **2017**, *41*, 9314–9320. https://doi.org/10.1039/C6NJ04070E.
11. Wang, X.; Wang, A.; Ma, J. Visible-light-driven photocatalytic removal of antibiotics by newly designed C_3N_4@$MnFe_2O_4$-graphene nanocomposites. *Journal of Hazardous Materials* **2017**, *336*, 81–92. https://doi.org/10.1016/j.jhazmat.2017.04.012.